

Double-sphere enhanced optomechanical spectroscopy constrains symmetron dark energy

Jiawei Li and Ka-Di Zhu*

*Key Laboratory of Artificial Structures and Quantum Control (Ministry of Education),
School of Physics and Astronomy, Shanghai Jiao Tong University,
800 DongChuan Road, Shanghai 200240, China*

(Dated: March 6, 2026)

Screened scalar fields such as the symmetron provide a viable description of dark energy yet their laboratory detection remains challenging. We propose an optomechanical scheme to constrain symmetron interactions using two optically levitated nanospheres inside a cavity. The symmetron-mediated interaction induces an effective coupling which leads to a measurable splitting in the optomechanical resonance spectrum. We forecast constraints in the regime $\mu \sim 10^{-2}\text{eV} - 10^{-4}\text{eV}$, which shows that this approach can improve existing laboratory bounds by up to several orders of magnitude, demonstrating the sensitivity of optomechanical spectroscopy to screened fifth forces.

I. INTRODUCTION

The accelerating expansion of universe has been confirmed by a variety of observation results including cosmic microwave background measurements [1, 2], type Ia supernovae [3, 4], and analyses of large-scale structure [5, 6]. These observations are well described within the framework of the Λ cold dark matter (Λ CDM) cosmological model [7–11]. However, it is disconcerting that there exists a discrepancy of about 60 orders of magnitude between the observed vacuum energy density, $\rho_{\Lambda}^{\text{obs}} \sim 10^{-120} M_{\text{Pl}}^4$, and its theoretical expectation from quantum zero-point fluctuations, $\rho_{\Lambda}^{\text{theo}} \sim 10^{-60} M_{\text{Pl}}^4$ with cutoff $\Lambda \sim 1\text{TeV}$ [12–17]. In addition, the apparent coincidence between the present vacuum energy density and the matter density also remains open problems, known as the coincidence problem [18, 19].

The smallness of the cosmological constant has often been interpreted from an anthropic perspective. In this view, a universe with a much larger vacuum energy would be unable to support the formation of large-scale structures and, consequently, the emergence of life [20]. While this anthropic argument provides a plausible selection effect, it does not offer a dynamical or physical explanation for the origin of cosmic acceleration, nor does it yield a predictive framework for the underlying structure of spacetime [21–25].

Cosmic acceleration can also arise from the potential energy of a slowly rolling scalar field, a scenario commonly referred to as quintessence [26–28]. However, such models are strongly constrained by local tests of gravity and the equivalence principle [29]. Moreover, the extremely weak coupling to matter required to satisfy these constraints often reintroduces fine-tuning problems, thereby limiting the theoretical appeal of these scenarios [30, 31].

An alternative approach is provided by scalar–tensor theories of gravity, which originate from early works by

Jordan, Brans and Dicke, and Bergmann [32–34]. As modifications of general relativity, these theories allow scalar fields to couple to matter and generically predict the existence of a so-called fifth force with observable consequences on cosmological scales [12, 35]. In high-density environments, however, such effects can be strongly suppressed, ensuring consistency with precision tests of general relativity in the solar system and in laboratory experiments [36–38]. The way to hide scalar fields from local laboratory detection, named as screening mechanism, which can be broadly classified based on the relation to the local field value ϕ . The first class of screening mechanisms is governed by a potential $V(\phi)$, including the symmetron [38], chameleon [39], and dilaton [40]. And the second class is based on $\partial\phi$ to shut off the fifth force, such as K-mouflage [41] and P(x) models [42]. Finally, the last class considering $\partial^2\phi$ involves the Vainshtein [43] and Galileon theories [44].

In this work we focus on the symmetron model, which can be regarded as a concrete realization of the Damour-Polyakov mechanisms [45–47]. To be specific, it relies on a \mathbb{Z}_2 -symmetric action of the symmetry-breaking form, under which whether the \mathbb{Z}_2 symmetry is spontaneously broken depends on the local matter density the scalar field ϕ couples to. In high density environment, the effective field potential has only one minimum and remains zero. While in the region with density lower than a critical value, the symmetry is spontaneously broken and ϕ acquires a vacuum expectation value $\phi = \pm\mu/\sqrt{\lambda}$ [35, 38, 48]. Existing constraints already exclude sizable regions of parameter space by variety of experiment design in both cosmical scales and tabletop experiments, including Casimir-force detection [49–51], quantum non-locality tests [52], astronomy detection [53–55], torsion pendulum experiments [56–58], neutron tests [59, 60] and atomic interferometry [48, 61–63].

The purpose of the present work is to establish constraints by utilizing a detection strategy based on optomechanical systems. In contrast to conventional force-measurement techniques, our approach exploits the modification of mechanical resonance frequencies induced by the symmetron-mediated interaction. The proposed

* zhukadi@sjtu.edu.cn

scheme provides a stronger constraints by up to $1 \sim 4$ orders of magnitude across a broad region of the symmetron parameter space within the region of μ in $10^{-2}\text{eV} \sim 10^{-4}\text{eV}$, complementing existing laboratory and astrophysical bounds. This paper is organized as follows. In Sec. II A, we briefly review the symmetron mechanism and derive the scalar field profile and fifth force generated by a spherically symmetric source mass. In Sec. II B, we introduce the optomechanical system considered in this work and show how the symmetron-induced interaction modifies the effective Hamiltonian of the coupled optical and mechanical modes. In Sec. III A, we discuss the choice of simulation experimental parameters and estimate the influence of environmental effects to our hypothetical experiment. In Sec. III B, we present the resulting constraints on the symmetron parameter space. Finally, Sec. IV summarizes our results and outlines prospects for future improvements.

II. MODEL AND THEORY

A. The symmetron screening mechanism

Generally speaking, the action of a scalar-tensor theory can be written in the form [64]

$$S = \int d^4x \sqrt{-g} \left(\frac{M_{\text{Pl}}^2}{2} R - \frac{1}{2} (\partial\phi)^2 - V(\phi) \right) + S_{\text{matter}} [A^2(\phi) g_{\mu\nu}, \psi], \quad (1)$$

in which R is the Ricci scalar associated with the Einstein-frame metric $g_{\mu\nu}$, and $V(\phi)$ is the scalar-field potential. Matter fields ψ are coupled to the Jordan-frame metric $\tilde{g}_{\mu\nu} = A^2(\phi) g_{\mu\nu}$ which introduces an effective coupling between matter and the scalar field through the conformal factor $A(\phi)$.

Considering a non-relativistic matter source, we note that the equation of motion for ϕ derived from Eq. (1) is

$$\square\phi = \frac{dV_{\text{eff}}(\phi)}{d\phi}, \quad (2)$$

where $V_{\text{eff}}(\phi) = V(\phi) + A(\phi)\rho$. Note that the scalar field can be dynamically suppressed in regions of high density by suitably choosing the potential and coupling to matter, by which the screening mechanism works.

For the symmetron, the simplest incarnation of this mechanism with a \mathbb{Z}_2 -symmetric action of the symmetry-breaking form is [38, 65]

$$S = \int d^4x \sqrt{-g} \left(\frac{M_{\text{Pl}}^2}{2} R - \frac{1}{2} (\partial\phi)^2 + \frac{\mu^2}{2} \phi^2 - \frac{\lambda}{4} \phi^4 \right) + S_{\text{matter}} \left[\left(1 + \frac{\phi^2}{2M^2} \right)^2 g_{\mu\nu} \right], \quad (3)$$

with the potential

$$V(\phi) = -\frac{\mu^2}{2} \phi^2 + \frac{\lambda}{4} \phi^4, \quad (4)$$

and the conformal factor given by

$$A(\phi) = 1 + \frac{\phi^2}{2M^2} + \mathcal{O}\left(\frac{\phi^4}{M^4}\right), \quad (5)$$

in which the model is governed by two parameters μ and M in mass scales as well as another dimensionless coupling parameter λ . Here, we drop the high order term since the parameter M is some high mass scale that ($\phi \ll M$). And then it is clear that the effective potential in Eq. (2) felt by ϕ in the non-relativistic scenario is given by

$$V_{\text{eff}}(\phi) = \frac{1}{2} \left(\frac{\rho}{M^2} - \mu^2 \right) \phi^2 + \frac{\lambda}{4} \phi^4. \quad (6)$$

Moreover, in vacuum, we consider a spherically symmetric, static, homogeneous, pressureless source of radius R ($\tilde{T} \simeq -\tilde{\rho}$). The equation of motion Eq. (2) describing the associated scalar field in spherical coordinates reduces to

$$\frac{d^2\phi}{dr^2} + \frac{2}{r} \frac{d\phi}{dr} = \frac{dV_{\text{eff}}(\phi)}{d\phi} \quad (7)$$

The boundary conditions require that the solution be smooth at the origin and approach its vacuum expectation value $\phi_0 = \mu/\sqrt{\lambda}$ at infinity,

$$\frac{d\phi}{dr}(0) = 0, \quad \phi(r \rightarrow \infty) = \phi_0. \quad (8)$$

With the above boundary conditions, the interior and exterior solutions of Eq.(7) are given by

$$\phi(r) = \frac{B}{r} \sinh\left(\sqrt{\alpha} \frac{r}{R}\right), \quad r < R. \quad (9)$$

$$\phi(r) = \phi_0 + \frac{C}{r} \exp\left(-\sqrt{2}\mu r\right), \quad r > R, \quad (10)$$

where $\alpha = \rho R^2/M^2$ is introduced as the thin-shell factor characterizing the screening strength, and B and C are two undetermined constants.

The coefficients B and C are determined by imposing the continuity of the scalar field and its derivative at the interface $r = R$. The resulting expressions are

$$B = \phi_0 R \frac{\sinh(\sqrt{\alpha}) - \sqrt{\alpha} \cosh(\sqrt{\alpha})}{\sqrt{\alpha} \cosh(\sqrt{\alpha}) + \sqrt{2}\mu R \sinh(\sqrt{\alpha})} \quad (11)$$

and

$$C = \phi_0 R \frac{1 + \sqrt{2}\mu R}{\sqrt{\alpha} \cosh(\sqrt{\alpha}) + \sqrt{2}\mu R \sinh(\sqrt{\alpha})}. \quad (12)$$

In this work, we focus on the symmetron-induced fifth force in the thin-shell limit ($\alpha \gg 1$), Eq.(10) reduces to

$$\phi \simeq \phi_0 - \phi_0 \left(1 - \frac{1}{\sqrt{\alpha}} \right) \frac{R}{r} \exp\left[-\sqrt{2}\mu(r - R)\right]. \quad (13)$$

For $\mu r \ll 1$, the exterior solution in the far field region ($R \ll r$) for two dense spheres further simplifies to

$$\phi \simeq \phi_0 - \phi_0 \frac{R}{r}. \quad (14)$$

Considering Eq. (5), the acceleration induced by the symmetron fifth force on a test object can be expressed in terms of the scalar field as

$$\mathbf{a} = -\frac{d \ln A(\phi)}{d\phi} \nabla \phi \approx -\frac{1}{M^2} \phi \nabla \phi \quad \phi \ll M. \quad (15)$$

Substituting Eq. (14) into Eq. (15), one can derive the fifth force sourced from a strongly screened sphere to a test object with mass m_{test} by:

$$F_s = \frac{m_{\text{test}} \phi_0^2 R}{M^2 r^2}. \quad (16)$$

We now return to Eq. (10) and consider the thick-shell limit $\alpha \ll 1$. In this case, the scalar field profile can be approximated as

$$\phi \simeq \phi_0 - \phi_0 \frac{\alpha R}{3 r} \exp\left[-\sqrt{2} \mu(r - R)\right], \quad (17)$$

which further simplifies in the regime $\mu r \ll 1$ to

$$\phi \simeq \phi_0 - \phi_0 \frac{\alpha R}{3 r}. \quad (18)$$

Substituting Eq. (18) into Eq. (15), the fifth force of non-screened source with m_{source} is:

$$F_{\text{ns}} = \frac{m_{\text{test}} m_{\text{source}} \phi_0^2}{4\pi M^4 r^2}. \quad (19)$$

Comparing Eqs. (16) and (19), one finds that the fifth force is suppressed by a factor $\lambda_{\text{sphere}} = 3M^2/\rho R^2$. Physically, this reflects the fact that the fifth force is no longer proportional to the total mass of the sphere, but only to a fraction $\lambda_{\text{sphere}} \ll 1$. Additionally, The source and test objects are strongly screened equally in this work. Consequently, for a system consisting of two strongly screened spheres, the interaction fifth force takes the form[51]

$$F = F_{\text{ns}} \times \lambda_{\text{source}} \lambda_{\text{test}} = \frac{4\pi R_{\text{source}} R_{\text{test}} \phi_0^2}{r^2}. \quad (20)$$

B. The cavity optomechanical system

Our scheme consider a system shown in Fig. 1. Two uniform fused silica spheres A and B are optically trapped at the center of the cavity with intrinsic vibration frequency ω_a and ω_b . The two spheres are separated by a gold-coated SiC membrane, which serves to suppress electrostatic and Casimir background forces by preventing direct electromagnetic coupling between the spheres [66, 67]. The membrane, with a thickness of $\sim 10\text{nm}$ is expected to be sufficiently stiff as reported

in the previous works [68–70]. The left mirror, the sphere A and the high-reflection membrane construct a new cavity, and we only consider the optomechanical interaction Hamiltonian between the light and the sphere A in the following part. We utilized a pump light with frequency ω_p and a relatively weak probe light with frequency ω_{pr} [71–73].

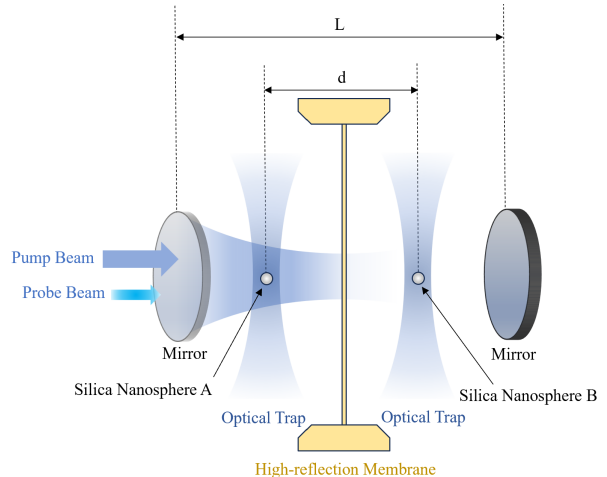


FIG. 1. Schematic diagram of the experimental setup. The system consists of two optically trapped silica nanospheres (A and B) with the same radius $R = 0.5\mu\text{m}$, which are confined inside a Fabry-Pérot cavity formed by two mirrors separated by a distance L . A strong pump beam together with a weak probe beam is injected through the left mirror to drive and probe the cavity field. These two nanospheres are localized at the opposite sides of a high-reflection membrane placed at the cavity center. The distance between the two nanospheres is denoted by $d = 4\mu\text{m}$. And the membrane also serves as a reflective mirror that isolates the two trapping regions.

The free Hamiltonian of the system are given as follows: $H_{\text{free}} = \hbar\omega_a \hat{\sigma}_a^\dagger \hat{\sigma}_a + \hbar\omega_b \hat{\sigma}_b^\dagger \hat{\sigma}_b + \hbar\omega_{\text{cav}} \hat{a}^\dagger \hat{a}$, consisting of the free Hamiltonian of sphere A, B and the cavity mode ω_{cav} . Here \hat{a} , $\hat{\sigma}_a$ and $\hat{\sigma}_b$ are the annihilation operators of the cavity mode and the two mechanical modes, respectively. In a frame rotating at the pump frequency, the total Hamiltonian of the system takes the form [74, 75]

$$H = \hbar\Delta_{\text{pu}} \hat{a}^\dagger \hat{a} + \hbar\omega_a \hat{\sigma}_a^\dagger \hat{\sigma}_a + \hbar\omega_b \hat{\sigma}_b^\dagger \hat{\sigma}_b + \hbar g \hat{a}^\dagger \hat{a} (\hat{\sigma}_a^\dagger + \hat{\sigma}_a) - i\hbar\Omega_p (\hat{a} - \hat{a}^\dagger) - i\hbar\Omega_{\text{pr}} (\hat{a} e^{i\delta t} - \hat{a}^\dagger e^{-i\delta t}) + H_{\text{int}}. \quad (21)$$

Here $\Delta_{\text{pu}} = \omega_{\text{cav}} - \omega_p$ is the pump-cavity detuning and $\delta = \omega_{\text{pr}} - \omega_p$ is the pump-probe detuning. And $\Omega_p = \sqrt{2P_p \kappa / \hbar\omega_p}$, $\Omega_{\text{pr}} = \sqrt{2P_{\text{pr}} \kappa / \hbar\omega_{\text{pr}}}$ are the Rabi frequencies of the pump and probe fields, respectively. The optomechanical interaction between the dielectric nanosphere A and the cavity field is described by the coupling Hamiltonian $\hbar g \hat{a}^\dagger \hat{a} (\hat{\sigma}_a^\dagger + \hat{\sigma}_a)$, where g is the coupling strength. The last term H_{int} accounts for the symmetron-induced interaction potential energy between the two levitated spheres A and B.

Considering Eq. (20), the resulting potential energy is given by

$$V(r) = -\frac{4\pi R_{\text{source}} R_{\text{test}} \phi_0^2}{r}. \quad (22)$$

Here the distance between the two spheres can be written as $r = d + x_a - x_b$, where $x_{a,b}$ stand for the displacements of the spheres A and B from their equilibrium positions. Expanding Eq. (22) to second order in the small displacements $|x_a|, |x_b| \ll d$, one obtains

$$V(r) \simeq -4\pi R_{\text{source}} R_{\text{test}} \phi_0^2 \left[\frac{1}{d} - \frac{x_a - x_b}{d^2} + \frac{(x_a - x_b)^2}{d^3} \dots \right] \quad (23)$$

For Eq. (23), One can find the first term remain constant, while the second term corresponds to a steady force that does not contribute to the interaction dynamics [76]. The third term, with second order of $x_a - x_b$, describes a coupling between the motions of the two spheres. Considering only the lowest-order coupling term, the interaction Hamiltonian can be obtained by quantization of the mechanical degrees of freedom of spheres A and B. With the rotating-wave approximation, we have

$$\begin{aligned} H_{\text{int}} &= -8\pi R_{\text{source}} R_{\text{test}} \phi_0^2 x_a x_b \\ &\simeq \hbar \Omega \left(\hat{\sigma}_a^\dagger \hat{\sigma}_b + \hat{\sigma}_a \hat{\sigma}_b^\dagger \right), \end{aligned} \quad (24)$$

where the coupling strength is given by

$$\Omega = -\frac{8\pi R_{\text{source}} R_{\text{test}} \phi_0^2}{\hbar d^3} \sqrt{\frac{\hbar}{2m_a \omega_a}} \sqrt{\frac{\hbar}{2m_b \omega_b}} \quad (25)$$

$$= -\frac{4\pi R_{\text{source}} R_{\text{test}} \mu^2}{\lambda d^3} \sqrt{\frac{1}{m_a m_b \omega_a \omega_b}} \quad (26)$$

The coefficient Ω is defined as the strength of the symmetron-induced interaction between the two spheres, with the dimension of frequency.

Then we define the operators $s_i = \hat{\sigma}_i^\dagger + \hat{\sigma}_i$ ($i = a, b$), which describe the position quadratures of the mechanical oscillators. By considering the commutation relations that $[\hat{\sigma}_i, \hat{\sigma}_i^\dagger] = 1$ and $[a, a^\dagger] = 1$, substituting Eqs. (21) and (26) into the Heisenberg equations of motion, we have the mean field evolution of s_i and a described by the quantum Langevin equations with additional damping terms:

$$\begin{aligned} \frac{d\langle \hat{a} \rangle}{dt} &= -(i\Delta_{\text{pu}} + \kappa) \langle \hat{a} \rangle + ig\langle s_a \rangle \langle \hat{a} \rangle + \Omega_p + \Omega_{\text{pr}} e^{-i\delta t}, \\ &+ \sqrt{\kappa_{\text{ex}}} \langle \hat{a}_{\text{in}} \rangle + \sqrt{\kappa_0} \langle \hat{f}_{\text{in}} \rangle, \end{aligned} \quad (27)$$

$$\begin{aligned} \frac{d^2 \langle s_a \rangle}{dt^2} + \gamma_1 \frac{d\langle s_a \rangle}{dt} + (\omega_a^2 + \Omega^2) \langle s_a \rangle - \Omega(\omega_a + \omega_b) \langle s_b \rangle \\ = 2g\omega_a \langle \hat{a}^\dagger \rangle \langle \hat{a} \rangle + \langle \hat{\xi} \rangle, \end{aligned} \quad (28)$$

$$\begin{aligned} \frac{d^2 \langle s_b \rangle}{dt^2} + \gamma_2 \frac{d\langle s_b \rangle}{dt} + (\omega_b^2 + \Omega^2) \langle s_b \rangle - \Omega(\omega_a + \omega_b) \langle s_a \rangle \\ = -2g\Omega \langle \hat{a}^\dagger \rangle \langle \hat{a} \rangle + \langle \hat{\xi} \rangle. \end{aligned} \quad (29)$$

Here $\kappa = \kappa_0 + \kappa_{\text{ex}}$ denotes the total cavity decay rate, and γ_i ($i = a, b$) are the damping rates of the mechanical modes of the spheres. The Langevin noise operator $\hat{a}_{\text{in}}(t)$ and \hat{f}_{in} represent the quantum and thermal noise operators associated with the optical and mechanical dissipation channels, respectively. With correlation function written as $\langle \hat{O}(t) \hat{O}(t_0) \rangle \sim \delta(t - t_0)$, these operators are supposed to have the mean value $\langle \hat{a}_{\text{in}}(t) \rangle = \langle \hat{f}_{\text{in}}(t) \rangle = 0$. The operator $\hat{\xi}$ accounts for the influence of the thermal bath arising from non-Markovian stochastic processes and Brownian motion [75, 77]. It also has a zero mean value with correlation function is given by $\langle \xi(t)^\dagger \xi(t') \rangle = \gamma \omega \int 1/2\pi \omega e^{-i\omega(t-t')} [1 + \coth(\hbar\omega/2k_b T)] d\omega$.

To solve Eqs.(27)-(29), we introduce the following ansatz [78]:

$$\langle \hat{a}(t) \rangle = a_0 + a_+ e^{-i\delta t} + a_- e^{i\delta t}, \quad (30)$$

$$\langle s_a(t) \rangle = s_{a0} + s_{a+} e^{-i\delta t} + s_{a-} e^{i\delta t}, \quad (31)$$

$$\langle s_b(t) \rangle = s_{b0} + s_{b+} e^{-i\delta t} + s_{b-} e^{i\delta t}. \quad (32)$$

Taking Eqs.(30)–(32) into Eqs.(27)–(29) and dropping high order terms with weak probe Ω_{pr} , one can obtain the following equations with the same time dependence:

$$s_{a+} = \frac{\Omega(\omega_a + \omega_b) s_{b+} + 2g\omega_a (a_0^* a_+ + a_0 a_+^*)}{-\delta^2 - i\gamma_1 \delta + \omega_a^2 + \Omega^2}, \quad (33)$$

$$s_{a-} = \frac{\Omega(\omega_a + \omega_b) s_{b-} + 2g\omega_a (a_0^* a_- + a_0 a_-^*)}{-\delta^2 + i\gamma_1 \delta + \omega_a^2 + \Omega^2}, \quad (34)$$

$$s_{b+} = \frac{\Omega(\omega_a + \omega_b) s_{a+} - 2g\Omega (a_0^* a_+ + a_0 a_+^*)}{-\delta^2 - i\gamma_2 \delta + \omega_b^2 + \Omega^2}, \quad (35)$$

$$s_{b-} = \frac{\Omega(\omega_a + \omega_b) s_{a-} - 2g\Omega (a_0^* a_- + a_0 a_-^*)}{-\delta^2 + i\gamma_2 \delta + \omega_b^2 + \Omega^2}, \quad (36)$$

$$a_+ = \frac{\Omega_{\text{pr}} + ia_0 g s_{a+}}{i\Delta_{\text{pu}} + \kappa - i\delta - ig s_{a0}}, \quad (37)$$

$$a_- = \frac{ia_0 g s_{a-}}{i\Delta_{\text{pu}} + \kappa + i\delta - ig s_{a0}}, \quad (38)$$

$$a_0 = \frac{\Omega_p}{i\Delta_{\text{pu}} + \kappa - ig s_{a0}}, \quad (39)$$

$$(\omega_a^2 + \Omega^2) s_{a0} - \Omega(\omega_a + \omega_b) s_{b0} = 2g\omega_a |a_0|^2, \quad (40)$$

$$(\omega_b^2 + \Omega^2) s_{b0} - \Omega(\omega_a + \omega_b) s_{a0} = -2g\Omega |a_0|^2, \quad (41)$$

with the last three equations are the steady state equations which are time independent.

Solving the above equations one can obtain

$$a_+ = \frac{\Omega_{\text{pr}} [Z(W - X) + UN_0]}{Z(W^2 - X^2) + 2XUN_0}, \quad (42)$$

with the coefficient defined as follows: $W = \kappa - i\delta$, $X = i\Delta_{\text{pu}} - ig s_{a0}$, $Y_i = -\delta^2 - i\gamma_i \delta + \omega_i^2 + \Omega^2$ ($i = 1, 2$), $Z = Y_1 Y_2 - \Omega^2 (\omega_a + \omega_b)^2$, $U = 2ig^2 \omega_a Y_2 - 2ig^2 \Omega^2 (\omega_a + \omega_b)$. And here the cavity photon number $N_0 = |a_0|^2$ is obtained by solving $\Omega_p^2 = [\kappa^2 + (\Delta_{\text{pu}} - g s_{a0})^2] N_0$.

The final step of the optical calculation part is to calculate the transmission of the probe field. With the help of the input-output relation

$$\begin{aligned} a_{\text{out}}(t) &= a_{\text{in}}(t) - \sqrt{2\kappa}a(t) \\ &= (\Omega_p/\sqrt{2\kappa}e^{-i\omega_p t} + \Omega_s/\sqrt{2\kappa}e^{-i(\omega_p+\delta)t}) \\ &\quad - (\sqrt{2\kappa}a_0e^{-i\omega_p t} + \sqrt{2\kappa}a_+e^{-i(\omega_p+\delta)t} \\ &\quad + \sqrt{2\kappa}a_-e^{-i(\omega_p-\delta)t}). \end{aligned} \quad (43)$$

where a_{in} and a_{out} are the input drives and output fields operators.

Concentrate on the terms with frequency $\omega_{\text{pr}} = \omega_p + \delta$, we derive the transmission of the output probe field component, defined as the ratio of the output field and input field at the probe frequency [79]:

$$\mathcal{T}(\omega_s) = \frac{\Omega_s/\sqrt{2\kappa} - \sqrt{2\kappa}a_+}{\Omega_s/\sqrt{2\kappa}}. \quad (44)$$

III. NUMERICAL RESULTS

A. The detection of the frequency shift

This section aims to provide practical parameters and to demonstrate numerical results about the cavity transmission spectrum with noise analysis. For the optical system setup, we consider a cylindrical cavity of length $L = 31$ mm and mirror radius $R_c = 10$ mm, with the radius of curvature of the left mirror set to $R_L = 89$ mm. The cavity finesse is assumed to be $F = 30$, which corresponds to a decay rate $\kappa = \pi c/2FL = 4.98 \times 10^8$ Hz. The cavity resonance frequency is taken to be $\omega_{\text{cav}} = \omega_p$. For a pump beam with wavelength $\lambda = 1064$ nm and power $P_p = 1.9 \mu\text{W}$, the waist of the intracavity optical field and the corresponding Rabi frequency are estimated to be $w = 0.12$ mm and $\Omega_p \approx 10^{11}$ Hz, respectively [80]. On the mechanical side, the silica spheres A and B is set to have the same mass and volume that $m_a = m_b = 1.2 \times 10^{-15}$ kg, $V_a = V_b = 5.24 \times 10^{-19}$ m³, and also to oscillate at the same intrinsic frequency $\omega_a = \omega_b = 1.23 \times 10^6$ Hz [81]. And the trapping laser beam injected into the cavity is also chosen to have the wavelength $\lambda_{\text{laser}} = 1064$ nm and work at the power $P = 0.17$ W [82].

Based on the above parameters, several derived quantities can now be evaluated. The optomechanical coupling strength $g \approx 1.4$ Hz can be derived from [83]

$$g = \frac{3}{4} \frac{V_{\text{sphere}}}{V_c} \frac{\epsilon - 1}{\epsilon + 2} \omega_{\text{cav}}. \quad (45)$$

Here $\epsilon = 3.75$ is the relative permittivity for silica with $V_c = \pi L w^2/4$ is the cavity mode volume. We further estimate the air-molecule-induced mechanical damping rate of the spheres to be $\gamma_i \approx 1.5 \times 10^{-7}$ Hz ($i = a, b$) with

$$\gamma_i = \frac{3P}{R_i \rho_i v} \quad (46)$$

where $P = 10^{-10}$ torr represents is the residual gas pressure inside the cavity and $v = \sqrt{k_B T/m_{\text{gas}}}$ is the mean velocity of air molecules at temperature $T = 200$ K [83, 84].

Now we proceed to simulate the probe spectrum through Eq. (44) with all parameters determined. The results in \mathcal{T}^2 to $\delta - \omega_0$ spectra are shown in Fig. 2, where $\omega_0 = \omega_{a,b} = 1.23 \times 10^6$ Hz is the intrinsic frequency of sphere A and B. Firstly, in Fig. 2(a), we first consider the trivial case without fifth-force interaction ($\Omega = 0$), in which a single enhanced resonance peak appears at $\delta - \omega_0 = 0$.

Moreover, in Fig. 2(b) and Fig. 2(c), we present the spectral response when the symmetron-induced coupling between spheres A and B is included, with $\Omega = -2 \times 10^{-3}$ Hz and -4×10^{-3} Hz, respectively. To explain the phenomena, we introduce $|N\rangle$, $|n_1\rangle$, and $|n_2\rangle$ as the number states of the cavity photons, and the phonons of spheres A and B, respectively. In the absence of the fifth-force interaction ($\Omega = 0$), it can be found that The transition from $|N+1, n_1, n_2\rangle$ to $|N, n_1+1, n_2\rangle$ corresponds to the single eigenmode with eigenfrequency ω_0 . When the Hamiltonian is modified by the fifth-force term in Eq. (24), the eigen states of the system are instead replaced by the symmetric and antisymmetric hybrid states $|\pm\rangle$ of $|N, n_1+1, n_2\rangle$ and $|N, n_1, n_2+1\rangle$. These two hybrid states give rise to two new mechanical eigenmodes which correspond to eigen frequencies shifts by $\pm\Omega$ from the uncoupled mechanical frequency ω_0 . Thus, as shown in Fig. 2(b) and Fig. 2(c), the symmetron-induced coupling strength Ω has a simple relation to the frequency splitting ω_{sp} that

$$\omega_{sp} = 2\Omega \quad (47)$$

The frequency resolution of the system is determined by the full width at half maximum (FWHM) of the resonance peak, which is calculated to be $\omega_{\text{FWHM}} \approx 1.501 \times 10^{-7}$ Hz in Fig. 2(d). Therefore, the minimum resolvable peak splitting is estimated as $\omega_{sp} = 1.501 \times 10^{-7}$ Hz.

The next step is to analyze the system-level noise, which mainly consists of electromagnetic noise and thermomechanical noise. To characterize the electromagnetic contribution, we restrict our attention to the left optical cavity and consider only the coupling between sphere A and the shield membrane. Under this configuration, the system can be effectively described by a cavity optomechanical model in which the levitated microsphere and the membrane interact via an electrostatic dipole-dipole coupling. The corresponding interaction potential takes the form

$$U = -\frac{\mu_a \mu_S}{2\pi \epsilon_0 r^3}, \quad (48)$$

where μ_a and μ_S denote the electric dipole moments of the microsphere and the shield membrane, respectively. The instantaneous separation is expressed as $r' = d' + x_a - x_S$, where x_S represents the membrane displacement from equilibrium and $d' \approx 2 \mu\text{m}$ is the equilibrium distance between sphere A and the membrane

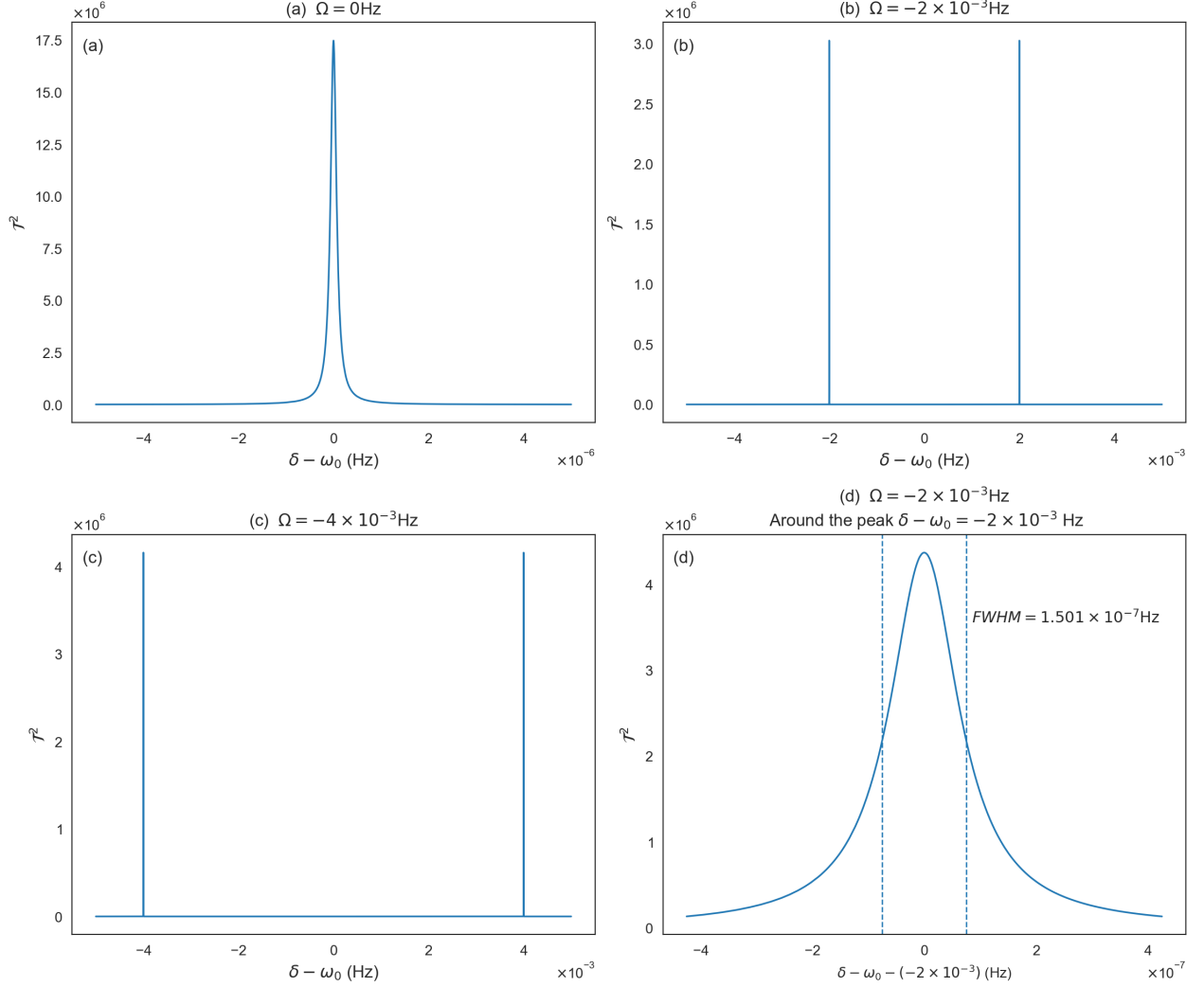


FIG. 2. Transmission \mathcal{T}^2 of the probe field as a function of $\delta - \omega_0$ for different values of the effective coupling parameter Ω . (a) In the absence of the symmetron-induced interaction ($\Omega = 0$), a single sharp resonance peak appears at $\delta - \omega_0 = 0$. (b) The original resonance splits into two distinct peaks located symmetrically around the central frequency for $\Omega = -2 \times 10^{-3}$ Hz. (c) The situation for $\Omega = -4 \times 10^{-3}$ Hz. (d) A magnified view of the resonance around $\delta - \omega_0 = -2 \times 10^{-3}$ Hz for $\Omega = -2 \times 10^{-3}$ Hz, where the full width at half maximum (FWHM) is extracted as 1.501×10^{-7} Hz, setting the achievable frequency resolution of the system.

surface [76]. Following the same procedure in Eqs. (22)-(26), we perform a Taylor expansion around $x_a - x_s \approx 0$, from which the dipole-interaction Hamiltonian can be obtained as

$$H_E \approx -\hbar\Psi \left(\hat{\sigma}_a^\dagger \hat{\sigma}_S + \hat{\sigma}_a \hat{\sigma}_S^\dagger \right), \quad (49)$$

with the coupling strength

$$\Psi = \frac{3\mu_i\mu_s}{\pi\epsilon_0 d'^5} \frac{1}{\sqrt{M_a M_s \omega_a \omega_s}}. \quad (50)$$

Here $\hat{\sigma}_S^\dagger$ ($\hat{\sigma}_S$) are the bosonic creation (annihilation) operators. The membrane is assumed to have mass $M_s \approx 6 \times 10^{-8}$ kg and mechanical frequency $\omega_s = 70$ MHz for a typical 1 cm-radius Au-coated SiC membrane [85]. While

the dipole moments are given by $\mu_a \approx 1.6 \times 10^{-23}$ C · m and $\mu_s \approx 1.6 \times 10^{-18}$ C · m [86]. With the above parameters, we can calculate the resulting coupling strength as $\Psi \approx 0.8$ Hz.

The total Hamiltonian of the system is then given by

$$H = \hbar\Delta_{\text{pu}}\hat{a}^\dagger\hat{a} + \hbar\omega_a\hat{\sigma}_a^\dagger\hat{\sigma}_a + \hbar\omega_s\hat{\sigma}_S^\dagger\hat{\sigma}_S + \hbar g\hat{a}^\dagger\hat{a}(\hat{\sigma}_a^\dagger + \hat{\sigma}_a) - i\hbar\Omega_p(\hat{a} - \hat{a}^\dagger) - i\hbar\Omega_{\text{pr}}(\hat{a}e^{i\delta t} - \hat{a}^\dagger e^{-i\delta t}) + H_E, \quad (51)$$

in which we apply the same treatment as what we did in Eqs. (21) and (27)-(43). And we plot the comparison when the influence of the membrane is considered or not in Fig. 3.

Despite the relatively large dipole coupling strength $\Psi \approx 0.8$ Hz, the probe transmission spectrum shows only

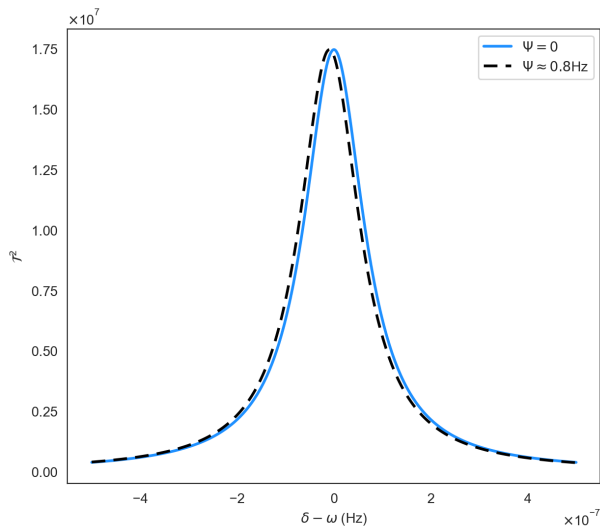


FIG. 3. The transmission resonance \mathcal{T}^2 of the probe field. The blue solid curve shows the situation without the consideration of dipole coupling ($\Psi = 0$), while the black dashed curve corresponds to the case with the coupling strength $\Psi \approx 0.8$ Hz. The two spectra almost overlap, showing only a very small frequency shift. This shift is far below the minimum resolvable frequency scale of $\sim 10^{-7}$ Hz and therefore does not affect the final sensitivity or the resulting constraints.

a negligible displacement owing to the substantial detuning between the resonance frequencies of ω_S and ω_a . The induced shift is well below the minimum frequency resolution of the system. Consequently, the electromagnetic noise of membrane can be neglected, enabling a clear observation of the symmetron-induced spectral splitting.

Here now we consider the thermomechanical noise. This noise originates from the stochastic thermal motion inherent to any realistic mechanical oscillator. Its impact on the measurement is characterized by the noise spectral density $S(\omega)$ together with the effective measurement bandwidth Δf [87]. For a one-dimensional harmonic oscillator with ω_n relevant to our system, the displacement spectral density $S_x(\omega)$ can be expressed as [88]

$$S_x(\omega) = \frac{S_F(\omega)}{m^2 [(\omega^2 - \omega_n^2)^2 + \omega^2 \omega_n^2 / Q^2]}. \quad (52)$$

Here, the force noise spectral density is given by $S_F(\omega) = 4m_{eff}\omega_n k_B T / Q$, where $k_B = 1.38 \times 10^{-23}$ J/K is the Boltzmann constant and $Q = \omega_a / 2\pi\gamma_a \approx 10^{12}$ the mechanical quality factor. The measurable bandwidth $\Delta f \approx 10^{-5}$ Hz is determined by the characteristic response time of the oscillator $\tau \approx 1.6 \times 10^4$ s through the relation $\Delta f \approx 1/(2\pi\tau)$ [76].

The minimum resolvable frequency shift is obtained by integrating the spectral density of frequency fluctuations, $S_\omega(\omega) = (\omega_n/2Q)^2 \cdot (S_x(\omega)/\langle x_{rms}^2 \rangle)$, over the frequency

window $\omega_n \pm \pi\Delta f$ [89, 90]. This procedure yields

$$\delta\omega \approx \sqrt{\frac{k_B T \Delta f}{m\omega_n \langle x_{rms} \rangle^2 Q}}. \quad (53)$$

Here, $\langle x_{rms} \rangle$ denotes the root-mean-square displacement for which the pump field remains within the predominantly linear response regime. For a pump beam with a Gaussian intensity profile and beam waist $w = 0.12$ mm, the displacement is given by $x_{rms} \ll \sqrt{w^2/2} = 84.8 \mu\text{m}$. Without loss of generality, we take $x_{rms} = 1 \mu\text{m}$ in the following analysis. Under this condition, the minimum detectable frequency shift limited by thermomechanical noise is estimated to be $\delta\omega_{min} \approx 4.32 \times 10^{-8}$ Hz, which is significantly smaller than the resonance linewidth $\omega_{FWHM} \approx 1.501 \times 10^{-7}$ Hz obtained in Sec. III A. Therefore, the influence of thermomechanical noise can be safely neglected.

B. Constraints on the symmetron

In this section, we establish constraints on the parameters of the symmetron model based on the results discussed in Sec. III A.

Before addressing the symmetron force constraints in detail, it is necessary to determine the range of feasible values of μ imposed by the geometry of the experimental setup. The lower bound on μ is related to the cavity length L along the resonant direction. In particular, the cavity mirrors on both sides should exert a negligible force on sphere A. The symmetron-induced force exerted by a single planar mass is given by [91, 92]

$$F = -\frac{4\pi\phi_0^2\mu R}{\sqrt{2}} \tanh\left(\frac{\mu x}{\sqrt{2}}\right) \text{sech}^2\left(\frac{\mu x}{\sqrt{2}}\right). \quad (54)$$

Here $x \approx L/2 = 1.55$ cm represent the distance from the source plate to the sphere. Requiring the mirror-induced force to be sufficiently suppressed leads to the condition $\mu L/2 > 1$, which sets the lower bound on μ . The upper bound on μ follows from the requirement $\mu d < 1$, as discussed in Eq. (14) [51, 93]. With $d = 4 \mu\text{m}$, the resulting feasible range of μ is $10^{-4} \text{eV} < \mu < 10^{-2} \text{eV}$.

Having fixed the allowed range of μ , we next establish constraints on the parameters M and λ . We first consider the M - μ parameter plane, which is primarily determined by the background matter density.

To ensure the calculation in Sec. II A and Eq.(54) remain valid, the critical density $\rho_{crit} = \mu^2 M^2$ should satisfy:

$$\rho_{vac} < \mu^2 M^2 < \rho_{sphere}, \quad (55)$$

by which the symmetron field value remains $\phi \sim 0$ everywhere inside the spheres and $\phi \sim \phi_0$ in the vacuum region inside the objects in the system. Here $\rho_{vac} \approx 2.2 \times 10^{-13} \text{kg} \cdot \text{m}^{-3}$ corresponds to the residual

air density at 10^{-10} torr vacuum and 200K and $\rho_{sphere} = 2.2 \times 10^3 \text{ kg} \cdot \text{m}^{-3}$ is the density of silica.

Additionally, the sphere are assumed to be strongly screened in Sec.II B, so that the thin-shell factor $\alpha > 1$ is required. Considering $\alpha = \rho R^2/M^2$, the constraint can be written as

$$\frac{\rho_{sphere} R^2}{M^2} > 1. \quad (56)$$

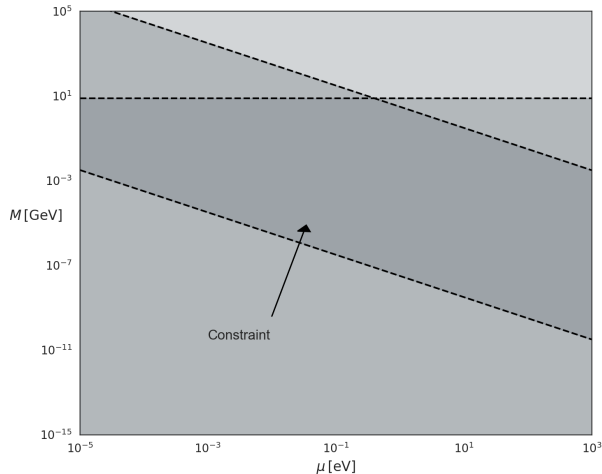


FIG. 4. Constraints on the symmetron parameters M and μ . The shaded regions correspond to parameter spaces restricted by different theoretical and physical requirements, while the overlap region highlighted in dark grey represents the final experimental allowed parameter space.

We illustrate the resulting constraints in Fig. 4 according to Eqs. (55) and (56). The horizontal line corresponds to the condition in Eq. (55), while the other two lines represent the limits on M imposed by Eq. (56). The central region shaded in dark grey indicates the constraints obtained.

The final step required for a complete constraint on the symmetron field is the determination of the parameter λ . The projected bound on λ follows directly from our optomechanical sensitivity via Eqs. (26) and (47). For fixed values of μ and M , a larger peak splitting ω_{sp} corresponds to a smaller λ . Consequently, only parameter values that predict a peak splitting exceeding $\omega_{sp}^{\text{lim}} = 1.501 \times 10^{-7} \text{ Hz}$ can be probed by our scheme, while smaller splittings remain experimentally inaccessible. In Fig. 5, we illustrate the value of the peak splitting ω_{sp} with different values of λ and μ . The white line with the label $\Omega_{sp} = 1.501 \times 10^{-7} \text{ Hz}$ refers to the detection limit of our system.

Before deriving the constraints discussed in Sec. III B, it is necessary to account for the suppressing effect of the membrane on the symmetron-mediated interaction acting on sphere B. A dense membrane placed between the source and probe objects attenuates the propagation of the scalar field through the material. In the high-density environment of the membrane, where ρ_{mbr} is large, the

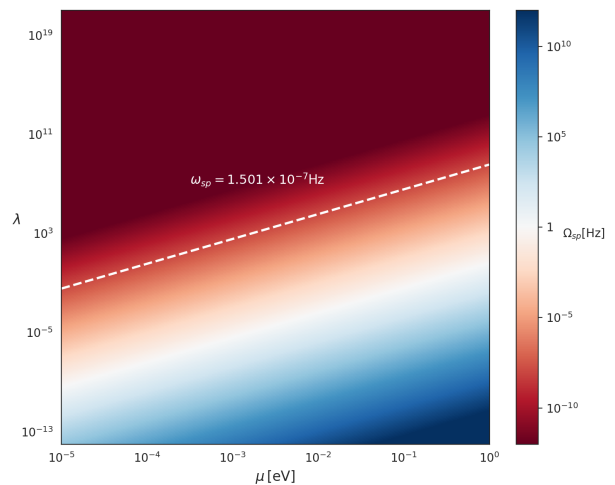


FIG. 5. Expected constraints on the symmetron parameters μ and λ . The color map shows the predicted frequency shift ω_{sp} induced by the symmetron interaction as a function of μ, λ . The white dashed line corresponds to the contour $\omega_{sp} = 1.501 \times 10^{-7} \text{ Hz}$, which represents the projected experimental sensitivity and thus defines the detectability threshold. Parameter regions above this curve yield splittings below the sensitivity limit and are therefore not accessible to our system.

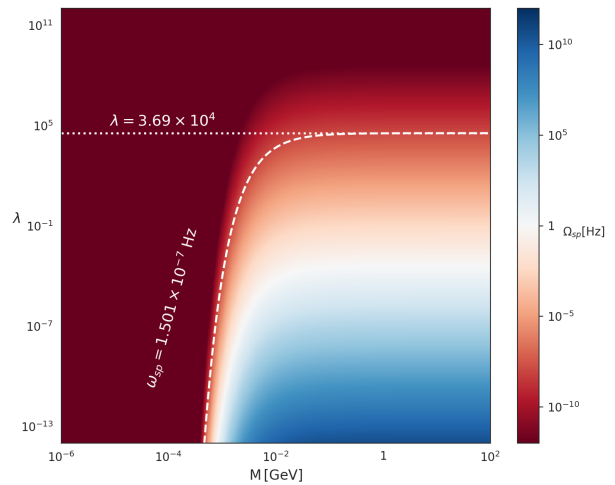


FIG. 6. Effect of membrane screening on the symmetron-induced peak splitting in the λ - M plane for a fixed $\mu = 10^{-2} \text{ eV}$. The color map shows the predicted splitting ω_{sp} including the suppression factor $e^{-2m_{\text{eff}}l_m}$. The white horizontal line with label $\lambda = 3.69 \times 10^4$ represents the original constraint from Fig. 5, while the white dashed curve marks the sensitivity contour $\omega_{sp} = 1.501 \times 10^{-7} \text{ Hz}$.

symmetron field resides near the symmetry-restored configuration $\phi \simeq 0$, and small perturbations obey the following relation by dropping the high order terms

$$\nabla^2 \phi \simeq m_{\text{eff}}^2 \phi, \quad m_{\text{eff}} = \sqrt{\left| \frac{\rho_{\text{mbr}}}{M^2} - \mu^2 \right|}. \quad (57)$$

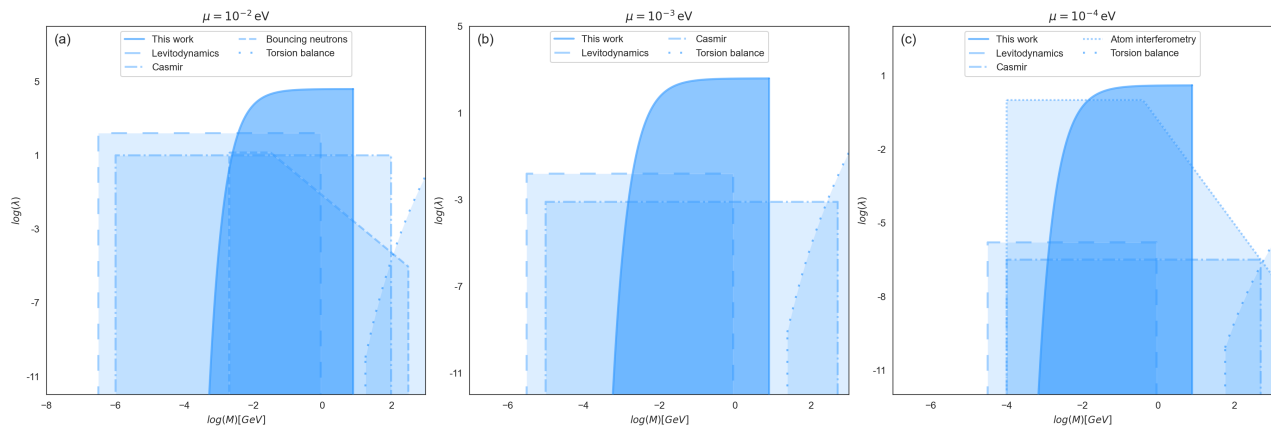


FIG. 7. Constraints on the symmetron parameter space from our proposed scheme, compared with bounds from Casimir-force, atom-interferometry, torsion-balance, ultracold neutron and Levitodynamics experiments [51, 57, 59, 91, 94]. The exclusion region is obtained from Figs. 5 and 6 for $\mu = 10^{-2}\text{eV}$, 10^{-3}eV , 10^{-4}eV .

Accordingly, the field amplitude across a membrane of thickness l_m is exponentially attenuated, which we parameterize by a factor $t_m \sim e^{-m_{\text{eff}} l_m}$ following the common treatment in torsion-balance estimates [57, 95].

For symmetron models the fifth-force acceleration depends quadratically on the field amplitude considering Eq. (15). So that if $\phi \rightarrow t_m \phi$ inside and beyond the membrane, then $\nabla \phi \rightarrow t_m \nabla \phi$ and the acceleration (or force signal) is suppressed as $a \rightarrow t_m^2 a$. We therefore define an effective screening factor for the symmetron-induced force,

$$f_{\text{scr}} \equiv t_m^2 \sim e^{-2m_{\text{eff}} l_m}, \quad (58)$$

which rescales the interaction-induced peak splitting.

Including this suppression factor, the peak splitting induced by the symmetron-mediated interaction becomes

$$\omega_{sp} = -\frac{8\pi R^2 \mu^2 f_{\text{scr}}}{\lambda m_a \omega_a}. \quad (59)$$

Taking $l_m \sim 10^{-2}\text{eV}^{-1}$ and $\rho_{\text{mbr}} \sim 10^{18}\text{eV}^4$ in natural units, we plot the relation between λ and M for a fixed value $\mu = 10^{-2}\text{eV}$ in Fig. 6. A sharp cutoff appears at small M , corresponding to the regime in which the membrane strongly suppresses the symmetron field, while for sufficiently large M the result approaches the unscreened limit shown in Fig. 5.

Fig. 7 summarizes the constraints obtained for several representative values of μ . The projected bounds from this work are shown in dark blue, while existing limits from other approaches are indicated by the light-blue shaded regions. These include the levitodynamics proposal [91], a Casimir-force-based design [51], atom interferometry experiments [94], torsion-balance measurements [57], and ultracold bouncing neutron experiments [59]. As illustrated in the figure, the scheme in this work provides stronger constraints especially for μ around 10^{-3}eV than the existing techniques, which are

largely complementary to other probes. Taken together, the collection of existing constraints and projected sensitivities covers a substantial fraction of the symmetron parameter space.

IV. CONCLUSION AND DISCUSSION

In this work, we propose an optomechanical approach to probe and constrain the symmetron-mediated fifth force. We consider a system consisting of two high-density spheres trapped inside an optical cavity and separated by a highly reflective membrane, and analyze the resulting symmetron field configuration in the presence of screening effects. Within the framework of quantum optics, we derive the transmission spectrum of the optomechanical system and characterize the dominant noise sources relevant for force detection. This analysis establishes a quantitative connection between the symmetron-induced interaction and the minimum resolvable spectral peak splitting. Based on the projected performance of the proposed setup, we obtain constraints on the symmetron parameter space that significantly improve existing bounds, achieving an enhancement of up to four orders of magnitude around $\mu = 10^{-3}\text{eV}$.

It is interesting to explore potential applications of our results to broader contexts, such as astrophysical phenomena including gravitational-wave detection [96, 97]. The optomechanical platform may also be relevant for next-generation experiments aimed at detecting ultra-weak effects associated with dark energy [98, 99]. Compared with our previous work in Ref. [91], the present scheme successfully raises the upper bound on the coupling parameter λ , as shown in Fig. 7. However, the accessible ranges of μ and M become narrower, mainly due to the suppressing effect introduced by the membrane. Alternative experimental designs may help to relax these constraints. Recent advances in coherent con-

trol of massive nanoparticles, including matter-wave interferometry [100] and quantum squeezing in levitated optomechanical systems [101], suggest that future extensions of our scheme could exploit similar techniques to improve coherence, increase test-mass size, and further enhance force sensitivity. In addition, employing non-spherical source or test masses could further enhance the sensitivity [102, 103], since optimized geometries, such as ellipsoids, are expected to suppress screening effects [93]. More accurate approximations for complex geometries may also lead to more reliable constraints [104, 105].

With continued advances in experimental techniques, we expect that optomechanics-based detection schemes will play an increasingly important role in testing screened dark energy models.

ACKNOWLEDGMENTS

This work is supported by Natural Science Foundation of Shanghai.

-
- [1] C. L. Chang, K. M. Huffenberger, B. A. Benson, *et al.*, Snowmass2021 cosmic frontier: Cosmic microwave background measurements white paper (2022), [arXiv:2203.07638 \[astro-ph.CO\]](#).
 - [2] A. Balbi, P. Ade, J. Bock, J. Borrill, *et al.*, Erratum: "constraints on cosmological parameters from maximall" (*apj* 545, 11 [2000]), *The Astrophysical Journal* **558**, L145 (2001).
 - [3] A. J. Ruiter and I. R. Seitzzahl, *Type ia supernova progenitors: a contemporary view of a long-standing puzzle* (2024), [arXiv:2412.01766 \[astro-ph.SR\]](#).
 - [4] S. Blondin, *Type ia supernovae* (2025), [arXiv:2411.09740 \[astro-ph.HE\]](#).
 - [5] M. Hameeda, B. Pourhassan, S. Masood, M. Faizal, L.-G. Wang, and S. Abass, The large-scale structure formation in an expanding universe, *International Journal of Modern Physics A* **37**, 2250086 (2022).
 - [6] S. Sarkar, *Impact of large-scale structure formation on the global information budget* (2024), [arXiv:2407.03042 \[astro-ph.CO\]](#).
 - [7] P. Brax, What makes the universe accelerate? a review on what dark energy could be and how to test it, *Reports on Progress in Physics* **81**, 016902 (2017).
 - [8] A. G. Riess, A. V. Filippenko, P. Challis, *et al.*, Observational evidence from supernovae for an accelerating universe and a cosmological constant, *The Astronomical Journal* **116**, 1009 (1998).
 - [9] B. P. Schmidt, N. B. Suntzeff, M. M. Phillips, *et al.*, The high-*z* supernova search: Measuring cosmic deceleration and global curvature of the universe using type ia supernovae, *The Astrophysical Journal* **507**, 46 (1998).
 - [10] J. P. Ostriker and P. J. Steinhardt, *Cosmic concordance* (1995), [arXiv:astro-ph/9505066 \[astro-ph\]](#).
 - [11] N. A. Bahcall, J. P. Ostriker, S. Perlmutter, and P. J. Steinhardt, The cosmic triangle: Revealing the state of the universe, *Science* **284**, 1481 (1999).
 - [12] A. Joyce, B. Jain, J. Khoury, and M. Trodden, Beyond the cosmological standard model, *Physics Reports* **568**, 1 (2015), beyond the cosmological standard model.
 - [13] L. Lombriser, On the cosmological constant problem, *Physics Letters B* **797**, 134804 (2019).
 - [14] H. E. S. Velten, R. F. vom Marttens, and W. Zimdahl, Aspects of the cosmological "coincidence problem", *The European Physical Journal C* **74** (2014).
 - [15] J. Solà, Cosmological constant and vacuum energy: old and new ideas, *Journal of Physics: Conference Series* **453**, 012015 (2013).
 - [16] A. Padilla, *Lectures on the cosmological constant problem* (2015), [arXiv:1502.05296 \[hep-th\]](#).
 - [17] S. Weinberg, The cosmological constant problem, *Rev. Mod. Phys.* **61**, 1 (1989).
 - [18] S. del Campo, R. Herrera, and D. Pavón, Toward a solution of the coincidence problem, *Phys. Rev. D* **78**, 021302 (2008).
 - [19] D. L. Gonçalves, Coincidence theory, in *Handbook of Topological Fixed Point Theory*, edited by R. F. Brown, M. Furi, L. Górniewicz, and B. Jiang (Springer Netherlands, Dordrecht, 2005) pp. 3–42.
 - [20] S. Weinberg, Anthropic bound on the cosmological constant, *Phys. Rev. Lett.* **59**, 2607 (1987).
 - [21] R. Bousso and J. Polchinski, Quantization of four-form fluxes and dynamical neutralization of the cosmological constant, *Journal of High Energy Physics* **2000**, 006 (2000).
 - [22] L. Susskind, *The anthropic landscape of string theory* (2003), [arXiv:hep-th/0302219 \[hep-th\]](#).
 - [23] C. G. Callan and S. Coleman, Fate of the false vacuum. ii. first quantum corrections, *Phys. Rev. D* **16**, 1762 (1977).
 - [24] A. Vilenkin, Birth of inflationary universes, *Phys. Rev. D* **27**, 2848 (1983).
 - [25] A. Vilenkin, Predictions from quantum cosmology, *Phys. Rev. Lett.* **74**, 846 (1995).
 - [26] S. Tsujikawa, Quintessence: a review, *Classical and Quantum Gravity* **30**, 214003 (2013).
 - [27] J. MARTIN, Quintessence: A mini-review, *Modern Physics Letters A* **23**, 1252 (2008).
 - [28] R. R. Caldwell and E. V. Linder, Limits of quintessence, *Phys. Rev. Lett.* **95**, 141301 (2005).
 - [29] V. Faraoni, Dark energy: Theory and observations, *Classical and Quantum Gravity* **28**, 049003 (2011).
 - [30] M. P. Hertzberg, M. Sandora, and M. Trodden, Quantum fine-tuning in stringy quintessence models, *Physics Letters B* **797**, 134878 (2019).
 - [31] C. Wetterich, The quantum gravity connection between inflation and quintessence, *Galaxies* **10**, 10.3390/galaxies10020050 (2022).
 - [32] P. Jordan, *Schwerkraft Und Weltall* (F. Vieweg, Braunschweig, 1955).
 - [33] C. Brans and R. H. Dicke, Mach's principle and a relativistic theory of gravitation, *Phys. Rev.* **124**, 925 (1961).
 - [34] P. G. Bergmann, Comments on the scalar tensor theory, *Int. J. Theor. Phys.* **1**, 25 (1968).

- [35] P. Brax, Screening mechanisms in modified gravity, *Classical and Quantum Gravity* **30**, 214005 (2013).
- [36] J. Khoury and A. Weltman, Chameleon fields: Awaiting surprises for tests of gravity in space, *Phys. Rev. Lett.* **93**, 171104 (2004).
- [37] J. Khoury, Theories of Dark Energy with Screening Mechanisms (2010), [arXiv:1011.5909](https://arxiv.org/abs/1011.5909) [astro-ph.CO].
- [38] K. Hinterbichler, J. Khoury, A. Levy, and A. Matas, Symmetron cosmology, *Phys. Rev. D* **84**, 103521 (2011).
- [39] J. Khoury and A. Weltman, Chameleon cosmology, *Phys. Rev. D* **69**, 044026 (2004).
- [40] J. García-Bellido, J. Rubio, M. Shaposhnikov, and D. Zenhäusern, Higgs-dilaton cosmology: From the early to the late universe, *Phys. Rev. D* **84**, 123504 (2011).
- [41] P. Brax and P. Valageas, k -mouflage cosmology: The background evolution, *Phys. Rev. D* **90**, 023507 (2014).
- [42] P. Brax, C. Burrage, and A.-C. Davis, Screening fifth forces in k -essence and dbi models, *Journal of Cosmology and Astroparticle Physics* **2013** (01), 020.
- [43] A. Vainshtein, To the problem of nonvanishing gravitation mass, *Physics Letters B* **39**, 393 (1972).
- [44] A. Nicolis, R. Rattazzi, and E. Trincherini, Galileon as a local modification of gravity, *Phys. Rev. D* **79**, 064036 (2009).
- [45] M. Pietroni, Dark energy condensation, *Phys. Rev. D* **72**, 043535 (2005).
- [46] P. Brax, A.-C. Davis, B. Li, and H. A. Winther, Unified description of screened modified gravity, *Phys. Rev. D* **86**, 044015 (2012).
- [47] T. Damour and A. Polyakov, The string dilation and a least coupling principle, *Nuclear Physics B* **423**, 532 (1994).
- [48] C. Burrage, A. Kuribayashi-Coleman, J. Stevenson, and B. Thrussell, Constraining symmetron fields with atom interferometry, *Journal of Cosmology and Astroparticle Physics* **2016** (12), 041.
- [49] R. S. Decca, D. López, E. Fischbach, G. L. Klimchitskaya, D. E. Krause, and V. M. Mostepanenko, Tests of new physics from precise measurements of the casimir pressure between two gold-coated plates, *Phys. Rev. D* **75**, 077101 (2007).
- [50] S. K. Lamoreaux, Demonstration of the casimir force in the 0.6 to $6\mu\text{m}$ range, *Phys. Rev. Lett.* **78**, 5 (1997).
- [51] B. Elder, V. Vardanyan, Y. Akrami, P. Brax, A.-C. Davis, and R. S. Decca, Classical symmetron force in casimir experiments, *Phys. Rev. D* **101**, 064065 (2020).
- [52] F. Feleppa, G. Lambiase, and S. Vagnozzi, Imprints of screened dark energy on nonlocal quantum correlations, *Phys. Rev. D* **112**, 084011 (2025).
- [53] T. Baker, A. Barreira, H. Desmond, P. Ferreira, B. Jain, K. Koyama, B. Li, L. Lombriser, A. Nicola, J. Sakstein, and F. Schmidt, Novel probes project: Tests of gravity on astrophysical scales, *Rev. Mod. Phys.* **93**, 015003 (2021).
- [54] M. Raveri, Reconstructing gravity on cosmological scales, *Phys. Rev. D* **101**, 083524 (2020).
- [55] Z.-X. Xiong and D. Huang, Gravitational wave birefringence in symmetron cosmology, *Phys. Rev. D* **111**, 084020 (2025).
- [56] D. J. Kapner, T. S. Cook, E. G. Adelberger, J. H. Gundlach, B. R. Heckel, C. D. Hoyle, and H. E. Swanson, Tests of the gravitational inverse-square law below the dark-energy length scale, *Phys. Rev. Lett.* **98**, 021101 (2007).
- [57] A. Upadhye, Symmetron dark energy in laboratory experiments, *Phys. Rev. Lett.* **110**, 031301 (2013).
- [58] Y.-L. Zhao, Y.-J. Tan, W.-H. Wu, J. Luo, and C.-G. Shao, Constraining the symmetron model with the hust-2020 torsion pendulum experiment, *Phys. Rev. Lett.* **129**, 141101 (2022).
- [59] G. Cronenberg, P. Brax, H. Filter, P. Geltenbort, T. Jenke, G. Pignol, M. Pitschmann, M. Thalhammer, and H. Abele, Acoustic rabi oscillations between gravitational quantum states and impact on symmetron dark energy, *Nature Physics* **14** (2018).
- [60] H. Fischer, C. Käding, H. Lemmel, S. Sponar, and M. Pitschmann, Search for dark energy with neutron interferometry, *Progress of Theoretical and Experimental Physics* **2024** (2024).
- [61] C. Burrage, E. J. Copeland, and E. Hinds, Probing dark energy with atom interferometry, *Journal of Cosmology and Astroparticle Physics* **2015** (03), 042.
- [62] P. Brax and A.-C. Davis, Atomic interferometry test of dark energy, *Phys. Rev. D* **94**, 104069 (2016).
- [63] M. Jaffe, P. Haslinger, V. Xu, P. Hamilton, A. Upadhye, B. Elder, J. Khoury, and H. Müller, Testing sub-gravitational forces on atoms from a miniature, in-vacuum source mass, *Nature Physics* **13** (2016).
- [64] J. D. Barrow, Scalar-tensor cosmologies, *Phys. Rev. D* **47**, 5329 (1993).
- [65] K. Hinterbichler and J. Khoury, Screening long-range forces through local symmetry restoration, *Phys. Rev. Lett.* **104**, 231301 (2010).
- [66] A. A. Geraci, S. J. Smullin, D. M. Weld, J. Chiaverini, and A. Kapitulnik, Improved constraints on non-newtonian forces at 10 microns, *Phys. Rev. D* **78**, 022002 (2008).
- [67] J. Chiaverini, S. J. Smullin, A. A. Geraci, D. M. Weld, and A. Kapitulnik, New experimental constraints on non-newtonian forces below 100 μm , *Phys. Rev. Lett.* **90**, 151101 (2003).
- [68] T. Nguyen, H. Phan, H. Kamble, R. K. Vadivelu, T. Dinh, A. Iacopi, G. M. Walker, L. Hold, N. Nguyen, and D. V. Dao, Superior robust ultrathin single-crystalline silicon carbide membrane as a versatile platform for biological applications., *ACS applied materials & interfaces* **9** **48**, 41641 (2017).
- [69] B. Morana, J. Creemer, F. Santagata, *et al.*, Lpcvd amorphous sicx for freestanding electron transparent windows (2010) pp. 572 – 575.
- [70] B. Lopez-Rodriguez, van der Kolk, *et al.*, High-quality amorphous silicon carbide for hybrid photonic integration deposited at a low temperature, *ACS Photonics* **10**, 3748 (2023).
- [71] L. Chen, J. Liu, and K.-D. Zhu, Constraining the axion-nucleon coupling and non-newtonian gravity with a levitated optomechanical device, *Phys. Rev. D* **106**, 095007 (2022).
- [72] A. A. Geraci, S. B. Papp, and J. Kitching, Short-range force detection using optically cooled levitated microspheres, *Phys. Rev. Lett.* **105**, 101101 (2010).
- [73] J. Liu and K.-D. Zhu, Nanogravity gradiometer based on a sharp optical nonlinearity in a levitated particle optomechanical system, *Phys. Rev. D* **95**, 044014 (2017).
- [74] C. Genes, D. Vitali, P. Tombesi, S. Gigan, and M. Aspelmeyer, Ground-state cooling of a micromechanical oscillator: Comparing cold damping and cavity-assisted

- cooling schemes, *Phys. Rev. A* **77**, 033804 (2008).
- [75] V. Giovannetti and D. Vitali, Phase-noise measurement in a cavity with a movable mirror undergoing quantum brownian motion, *Phys. Rev. A* **63**, 023812 (2001).
- [76] J. Liu and K.-D. Zhu, Cavity optomechanical spectroscopy constraints chameleon dark energy scenarios, *The European Physical Journal C* **78** (2018).
- [77] C. Gardiner and P. Zoller, *Quantum Noise: A Handbook of Markovian and Non-Markovian Quantum Stochastic Methods with Applications to Quantum Optics*, Springer Series in Synergetics (Springer, 2004).
- [78] R. Boyd and D. Prato, *Nonlinear Optics* (Elsevier Science, 2008).
- [79] W. Bowen and G. Milburn, *Quantum Optomechanics* (CRC Press, 2015).
- [80] P. Berman and V. Malinovsky, *Principles of Laser Spectroscopy and Quantum Optics* (Princeton University Press, 2011).
- [81] S. Groeblacher, K. Hammerer, M. Vanner, and M. Aspelmeyer, Observation of strong coupling between a micromechanical resonator and an optical cavity field, *Nature* **460**, 724 (2009).
- [82] U. Delić, D. Grass, M. Reisenbauer, T. Damm, M. Weitz, N. Kiesel, and M. Aspelmeyer, Levitated cavity optomechanics in high vacuum, *Quantum Science and Technology* **5**, 025006 (2020).
- [83] D. E. Chang, C. A. Regal, S. B. Papp, D. J. Wilson, J. Ye, O. Painter, H. J. Kimble, and P. Zoller, Cavity opto-mechanics using an optically levitated nanosphere, *Proceedings of the National Academy of Sciences* **107**, 1005 (2010).
- [84] D. Hunger, T. Steinmetz, Y. Colombe, C. Deutsch, T. W. Hänsch, and J. Reichel, A fiber fabry-perot cavity with high finesse, *New Journal of Physics* **12**, 065038 (2010).
- [85] A. R. Kermany, G. Brawley, N. Mishra, E. Sheridan, W. P. Bowen, and F. Iacopi, Microresonators with q-factors over a million from highly stressed epitaxial silicon carbide on silicon, *Applied Physics Letters* **104**, 081901 (2014).
- [86] A. D. Rider, D. C. Moore, C. P. Blakemore, M. Louis, M. Lu, and G. Gratta, Search for screened interactions associated with dark energy below the 100 μm length scale, *Phys. Rev. Lett.* **117**, 101101 (2016).
- [87] H. Mori, Statistical-Mechanical Theory of Kinetic Equations: Kinetic Equations for Dense Gases and Liquids, *Progress of Theoretical Physics* **49**, 1516 (1973).
- [88] K. L. Ekinci, Y. T. Yang, and M. L. Roukes, Ultimate limits to inertial mass sensing based upon nanoelectromechanical systems, *Journal of Applied Physics* **95**, 2682 (2004).
- [89] A. N. Cleland and M. L. Roukes, Noise processes in nanomechanical resonators, *Journal of Applied Physics* **92**, 2758 (2002).
- [90] W. P. Robins, Phase noise in signal sources: Theory and applications (1984).
- [91] J. Li and K.-D. Zhu, Constraining symmetron fields with a levitated optomechanical system, *Journal of Cosmology and Astroparticle Physics* **2025** (04), 036.
- [92] P. Brax and M. Pitschmann, Exact solutions to nonlinear symmetron theory: One- and two-mirror systems, *Phys. Rev. D* **97**, 064015 (2018).
- [93] L. Ogden, K. Brown, H. Mathur, and K. Rovelli, Electrostatic analogy for symmetron gravity, *Phys. Rev. D* **96**, 124029 (2017).
- [94] D. O. Sabulsky, I. Dutta, E. A. Hinds, B. Elder, C. Burrage, and E. J. Copeland, Experiment to detect dark energy forces using atom interferometry, *Phys. Rev. Lett.* **123**, 061102 (2019).
- [95] A. Upadhye, Dark energy fifth forces in torsion pendulum experiments, *Phys. Rev. D* **86**, 102003 (2012).
- [96] T. Guerreiro, Entanglement and squeezing of gravitational waves, *Phys. Rev. D* **112**, L101904 (2025).
- [97] X. Guo, H. Miao, Z.-W. Wang, H. Yang, and Y.-L. Zhou, Fundamental quantum limits for detecting ultra-high frequency gravitational waves, *Phys. Rev. D* **113**, 044020 (2026).
- [98] K. Clements, B. Elder, L. Hackermueller, M. Fromhold, and C. Burrage, Detecting dark domain walls through their impact on particle trajectories in tailored ultra-high vacuum environments, *Phys. Rev. D* **109**, 123023 (2024).
- [99] B. Elder and J. Sakstein, Constraining the chameleon-photon coupling with atomic spectroscopy, *Phys. Rev. D* **109**, 124007 (2024).
- [100] S. Gerlich *et al.*, Probing quantum mechanics with nanoparticle matter-wave interferometry, *Nature* **649**, 866 (2026).
- [101] M. Kamba, N. Hara, and K. Aikawa, Quantum squeezing of a levitated nanomechanical oscillator, *Science* **389**, 1225 (2025).
- [102] A. M. e. a. C. Burrage, E.J. Copeland, The shape dependence of chameleon screening, *Journal of Cosmology and Astroparticle Physics* **2018** (01), 056.
- [103] E. C. C. Burrage and J. Stevenson, Ellipticity weakens chameleon screening, *Phys. Rev. D* **91**, 065030 (2015).
- [104] P. Brax, C. van de Bruck, A.-C. Davis, D. F. Mota, and D. Shaw, Detecting chameleons through casimir force measurements, *Phys. Rev. D* **76**, 124034 (2007).
- [105] D. E. Krause, R. S. Decca, D. López, and E. Fischbach, Experimental investigation of the casimir force beyond the proximity-force approximation, *Phys. Rev. Lett.* **98**, 050403 (2007).